Thermally induced magnetization dynamics of optically excited YIG/Cu/$Ni_{81}Fe_{19}$ trilayers

H. J. Mohamad,[1,2] L. R. Shelford,[1] M. Aziz,[3] U. A. S. Al-Jarah,[1] R. Al-Saigh,[1] R. A. J. Valkass,[1] S. Marmion,[4] B. J. Hickey,[4] and R. J. Hicken[1]

[1]*Department of Physics and Astronomy, University of Exeter, Exeter EX4 4QL, United Kingdom*

[2]*Department of Physics, Al-Mustansiriyah University, Baghdad, Iraq*

[3]*Department of Engineering, University of Exeter, Exeter EX4 4QF, United Kingdom*

[4]*Department of Physics and Astronomy, University of Leeds, Leeds LS2 9JT, United Kingdom*

(Received 15 June 2017; revised manuscript received 26 September 2017; published 30 October 2017)

The response of $Y_3Fe_5O_{12}$/Cu/$Ni_{81}Fe_{19}$ trilayer structures to excitation by a femtosecond laser pulse has been studied in optical pump-probe experiments and compared with the response of $Y_3Fe_5O_{12}$ (YIG) and $Ni_{81}Fe_{19}$ reference samples. The optical pump induces a partial demagnetization of the $Ni_{81}Fe_{19}$, a large thermal gradient within the YIG, and temperature differences across the interfaces within the sample stack. When a moderate magnetic field is applied close to normal to the sample plane, so as to quasialign the YIG magnetization with the field and cant the $Ni_{81}Fe_{19}$ magnetization from the plane, ultrafast demagnetization initiates precession of the $Ni_{81}Fe_{19}$ magnetization. The transient temperature profile within the samples has been modeled using a one-dimensional finite-element computational model of heat conduction, while the magnetization dynamics are well described by a macrospin solution of the Landau-Lifshitz-Gilbert equation. The precessional response of the $Ni_{81}Fe_{19}$ layers within the trilayers and the $Ni_{81}Fe_{19}$ reference sample are very similar for pump fluences of up to 1.5 mJ/cm^2, beyond which irreversible changes to the magnetic properties of the films are observed. These results suggest that the spin Seebeck effect is ineffective in modifying the precessional dynamics of the present YIG/Cu/$Ni_{81}Fe_{19}$ samples when subject to ultrafast optical excitation.

DOI: 10.1103/PhysRevB.96.134431

I. INTRODUCTION

Pure spin currents, for which there is no associated transport of charge, have the potential to control a new generation of spintronic devices that are environmentally friendly and energy efficient. Spin currents carry angular momentum that can induce or modify magnetization dynamics by generating a spin transfer torque (STT) when absorbed by a ferromagnetic (FM) film. Electrical generation of spin currents has been achieved through spin diffusion in nonlocal transport devices [1] and by means of the spin Hall effect [2,3]. Alternatively, thermal generation of spin current can result from a class of spin Seebeck effects [4] (SSEs) and has been observed in spin-polarized metals [5], semiconductors [6], and insulators [7]. The SSE can be observed in thin films in transverse and longitudinal configurations where the direction of the temperature gradient, and hence the spin current, lies parallel and perpendicular to the plane of the film, respectively. While resistive heating elements may be deposited upon a thin film to perform electrical measurements of the transverse SSE, great care must be taken to separate out other parasitic effects [8]. On the other hand, a temperature gradient may easily be generated perpendicular to the plane by heating with a focused laser beam. The spin current generated by the longitudinal SSE (LSSE) has been detected by means of the inverse spin Hall effect in a Pt overlayer [9]. Most recently, the first direct optical measurements of spin current driven from a FM to a nonmagnetic layer, by an interfacial temperature difference, were reported [10].

Slonczewski suggested a scheme for optically induced magnetization reversal within a multilayered structure consisting of an insulating FM material such as a ferrite, a nonmagnetic metallic spacer layer, and a FM metal layer [11]. It was proposed that heating the ferrite layer could generate a magnon spin current by means of the LSSE. The spin current would then be carried through the spacer layer by spin-polarized conduction electrons, before being absorbed in the FM metal layer, generating a STT that could be used to switch the magnetization. The effect could be used either as the primary mechanism for writing data or for the optimization of an existing method such as heat-assisted magnetic recording. Optically induced magnetization dynamics are conveniently explored in all-optical pump-probe experiments. Recent studies have explored whether optical excitation of one FM layer in a metallic spin valve structure can generate spin currents that perturb the magnetization of the other FM layer [12–14]. The samples were designed so that the remanent magnetization lay out of the sample plane in the optically pumped FM layer, but in plane in the other FM layer, so as to maximize the strength of the Slonczewski-type STT. For these metallic structures, the LSSE is expected to arise mainly due to the spin-dependent Seebeck effect [5] (SDSE) rather than the SSE due to magnon transport [15]. However, if optical absorption occurs directly in the first FM layer, then STT associated with superdiffusive electron spin transport obscures that due to the smaller longitudinal SSE [12]. If optical absorption instead occurs in an optically thick nonmagnetic (NM) metallic layer directly adjoining the first FM layer, then ultrafast demagnetization can occur by transport of thermalized electrons from the NM to the first FM, with thermalized electrons also carrying spin angular momentum between the first and second FM layers [13]. A smaller but much longer lived (∼100 ps) STT can then arise due to the LSSE and is found to noticeably affect the phase of precession in the second FM layer [14]. In the present study, we instead explore $Y_3Fe_5O_{12}$/Cu/$Ni_{81}Fe_{19}$ spin valve structures in which the $Y_3Fe_5O_{12}$ (YIG) layer is an electrical insulator so that the effects of superdiffusive spin currents from the YIG

TABLE I. Composition of the samples studied. For samples T2 and T3 a piranha etch was applied to the surface of the YIG layer before deposition of the metallic overlayers.

Sample	Composition
R1	GGG/Cu (8 nm)/$Ni_{81}Fe_{19}$ (2 nm)/Al (2 nm)
R2	GGG/YIG (140 nm)/Cu (8 nm)/Al (2 nm)
T1	GGG/YIG (66.5 nm)/Cu (8 nm)/$Ni_{81}Fe_{19}$ (2 nm)/Al (2 nm)
T2	GGG/YIG (62 nm)/ Cu (8 nm)/$Ni_{81}Fe_{19}$ (2 nm)/Al (2 nm)
T3	GGG/YIG (62 nm)/Cu (3.5 nm)/Ta (1 nm)/Cu (3.5 nm)/$Ni_{81}Fe_{19}$ (2 nm)/Al (2 nm)

are eliminated and where the influence of a longitudinal SSE associated with magnons in the YIG layer can be assessed in the absence of the SDSE.

II. EXPERIMENTAL CONSIDERATION

The structure of the samples studied is shown in Table I. All samples were fabricated upon single-crystal $Gd_3Ga_5O_{12}$ gadolinium gallium garnet (GGG) substrates of (111) orientation. The GGG substrate has the same crystal structure as and similar lattice constant (1.2383 nm) to YIG (1.2376 nm), while the thermal expansion coefficients are also similar. The YIG was grown by RF sputtering in an argon/oxygen atmosphere, with 5% oxygen, at a pressure of 2.4 mTorr. The flow rates were 22.8 and 1.2 cm^3/min at STP for the argon and oxygen, respectively, while the growth rate was 0.22 Å/s. The samples were then annealed in air for 2 h, being heated to 850 °C at 7 °C per minute before being cooled at a similar rate to avoid damage of the film due to thermal shock. In some cases, a piranha etch [16] was applied to the surface of the YIG film after annealing to remove dead layers and improve surface quality. The samples were then placed back in the sputtering chamber for deposition of the metal layers. X-ray measurements were made on calibration samples to determine the sample thickness. It is now known that interdiffusion occurs at the GGG/YIG interface [17] but is limited to about 6 nm. Therefore, the YIG thickness was chosen to be ∼60 nm so that the upper part of the film had the composition of pure YIG. A copper layer thickness of 8 nm was chosen to eliminate any interlayer exchange coupling between the YIG and $Ni_{81}Fe_{19}$ layers, while being short compared to the spin diffusion length so that there should be negligible attenuation of the spin current while passing through the Cu layer. The absorption length for transverse spin current within the $Ni_{81}Fe_{19}$ is expected to be ∼1 nm [18] and so a thickness of 2 nm was chosen so that the spin current should be mostly absorbed and exert a large torque on the magnetic moment of the $Ni_{81}Fe_{19}$ layer. A control sample was fabricated with a 1-nm Ta layer in the middle of the Cu spacer to produce strong spin scattering and hence reduce the transport of spin angular momentum from YIG to $Ni_{81}Fe_{19}$.

All-optical pump-probe measurements were performed with a Ti:sapphire ultrafast regenerative amplifier laser system providing pulses of typically 74-fs duration at a repetition rate of 100 kHz. The 800-nm-wavelength pump beam was aligned at near normal incidence, while the frequency-doubled 400-nm probe beam was aligned 15° from the normal, with both beams passing through a conical hole in the pole piece of an electromagnet specifically designed for polar magneto-optical Kerr effect (MOKE) measurements [19]. The experimental geometry is shown in Fig. 1. The pump and probe beams had *s* and *p* polarization, respectively, and were focused to spots of 120 and 40 μm full width half maximum diameter, respectively, as determined by a laser beam profiler. The pump pulse is partially absorbed in the metallic overlayers of the sample, before passing through the optically transparent YIG and GGG. The electrons excited within the metal thermalize within a few hundred femtoseconds, at which point the electron temperature exceeds that of the lattice and maximum demagnetization of the $Ni_{81}Fe_{19}$ occurs [20]. The electron and lattice temperatures then converge on picosecond time scales and the magnetization of the $Ni_{81}Fe_{19}$ begins to recover as the electron temperature falls. A significant temperature difference is created initially across the YIG/Cu interface, which then falls as heat is transported into the YIG so that a large thermal gradient develops within the YIG layer. The temperature gradient is expected to generate a magnon spin current in the YIG, which is converted into an electronic spin current within the Cu layer. However, the temperature

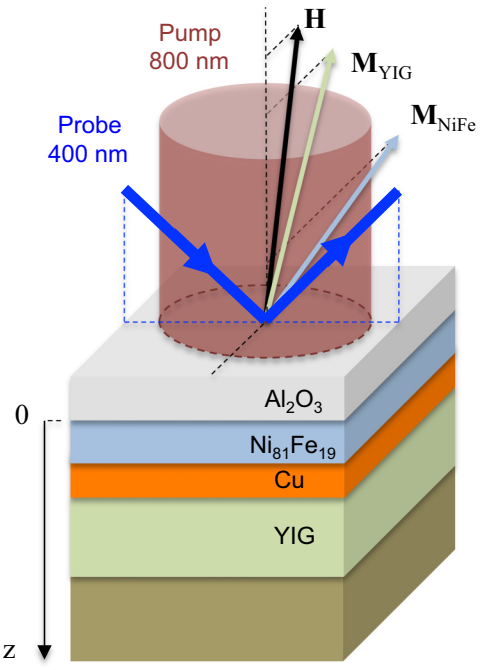

FIG. 1. Schematic representation of the optical pump-probe experiment.

difference across the YIG/Cu interface also leads to spin-flip scattering of electrons in the Cu from magnons in the YIG, producing a further contribution to the spin current. The total spin current is expected to pass through the Cu layer with minimal attenuation and then be absorbed within the $Ni_{81}Fe_{19}$ layer generating a STT.

The time-delayed probe pulse senses the total magnetic response of the sample structure by means of the MOKE. The probe beam was directed into an optical bridge detector in which a Glan-Thompson beam splitter directs two orthogonally polarized beams onto two photodiodes. The sum and difference of the two photodiode outputs are proportional to the intensity and Kerr rotation angle, respectively. The pump beam intensity was modulated with a mechanical chopper at 690 Hz and lock-in amplifiers used to measure the change in polarization and intensity induced by the pump. Due to the small angle of incidence, the measured Kerr rotation is predominantly due to the out-of-plane component of the magnetization via the polar MOKE, although the in-plane magnetization component that lies within the optical plane of incidence can also make a small contribution via the longitudinal MOKE.

Typically, measurements were performed with a magnetic field of 3 kOe applied at an angle of 2.8° relative to the film normal, with the in-plane field component perpendicular to the plane of incidence. This field is sufficient to quasialign the YIG magnetization with the field, while the Py magnetization is canted out of plane by the order of 20°. Ultrafast demagnetization then reduces the out-of-plane demagnetizing field associated with the $Ni_{81}Fe_{19}$ magnetization, modifying its equilibrium configuration and initiating precession. If the magnetic field is applied exactly normal to the plane of the sample, the precession frequency is very sensitive to any slight misalignment of the field orientation. For this reason, the field was deliberately misaligned by 2.8° so as to obtain a well-defined precession frequency. The large angle induced between the YIG and $Ni_{81}Fe_{19}$ magnetization is also expected to increase the initial Slonczewski STT acting upon the $Ni_{81}Fe_{19}$ so that its effect upon the precessional dynamics can be more easily observed.

III. THEORETICAL CONSIDERATION

Since the diameter of the focused probe spot is one-third that of the pump spot and also much larger than the thickness of the YIG/Cu/$Ni_{81}Fe_{19}$ trilayer, the magnetization dynamics may be reasonably described by a macrospin solution of the Landau-Lifshitz-Gilbert (LLG) equation with additional terms that describe STT. Assuming that the orientation of the YIG layer magnetization remains fixed, which will be justified by measurements to be presented for the YIG reference film R2, the LLG Slonczewski equation of motion for the $Ni_{81}Fe_{19}$ free layer in the macrospin limit may be written as

$$\frac{\partial \mathbf{M}}{\partial t} = -|\gamma|\mathbf{M}\times\mathbf{H}_{\text{eff}} + \frac{\alpha}{M}\mathbf{M}\times\frac{\partial \mathbf{M}}{\partial t} - a\mathbf{M}\times(\mathbf{M}\times\mathbf{p}) + b\mathbf{M}\times\mathbf{p}. \quad (1)$$

The first term on the right-hand side describes the torque on the $Ni_{81}Fe_{19}$ free layer magnetization $\mathbf{M}$ due to $\mathbf{H}_{\text{eff}}$, the sum of the external, anisotropy, and demagnetizing fields, while γ is the gyromagnetic ratio. The second term describes the Gilbert damping, where α is the dimensionless Gilbert damping parameter. The third and fourth terms represent the Slonczewski antidamping (in-plane) and fieldlike (out-of-plane) STT terms due to injection of a spin current and $\mathbf{p}$ is a unit vector parallel to the magnetization of the YIG. The fourth term is usually assumed to be negligible for metallic nonmagnetic spacer layers supporting diffusive transport and so is neglected in this work. The constant a determines the size of the antidamping torque and can be written as $a = |g|\mu_B\eta J_s/2edM$ [2], where g is the spectroscopic splitting factor, μ_B is the Bohr magneton, η is the efficiency of transfer of spin current from one layer to another, which ranges from 0 to 1, d is the thickness of the free layer, and J_s is the spin current density expressed in charge units.

Let us choose a Cartesian coordinate system in which the z axis lies normal to the film plane and the x axis lies parallel to the in-plane component of the external applied field $\mathbf{H}$, so that $H_y = 0$. The orientation of the magnetization may then be defined by the polar angle θ that it describes relative to the z axis and the azimuthal angle φ defined relative to the x axis. Any in-plane uniaxial anisotropy field is assumed to be small compared to the external applied field so that it may be neglected. The effective field acting on the magnetization then has components

$$H_{\text{eff},\varphi} = -H_x\sin\varphi, \quad (2)$$

$$H_{\text{eff},\theta} = H_x\cos\varphi\cos\theta - H_z\sin\theta + 4\pi M\cos\theta\sin\theta. \quad (3)$$

The equilibrium orientation of the magnetization in the absence of a spin current is found by setting the effective fields equal to zero, yielding

$$\varphi_0 = 0, \quad H_x\cos\theta_0 - H_z\sin\theta_0 + 4\pi M\cos\theta_0\sin\theta_0 = 0. \quad (4)$$

Assuming that the dynamic components of $\mathbf{M}$ and $\mathbf{H}_{\text{eff}}$ are small, Eq. (1) is expected to have harmonic solutions of the form

$$\theta = \theta_0 + \theta_1 e^{-i\omega t}, \quad \varphi = \varphi_1 e^{-i\omega t}, \quad (5)$$

where $\theta_1 \ll \theta_0$. After linearizing, Eq. (1) takes the form of simultaneous linear equations for θ_1 and φ_1, which have nonvanishing solutions when

$$\frac{\omega^2}{|\gamma|^2} = H_x(H_x\sin\theta_0 + H_z\cos\theta_0 - 4\pi M\cos 2\theta_0)/\sin\theta_0. \quad (6)$$

In the experimental configuration described within the preceding section, excitation of the sample by a femtosecond laser pulse leads to a time-dependent demagnetizing field associated with ultrafast demagnetization and recovery of the magnetization within the $Ni_{81}Fe_{19}$ layer and potentially a time-dependent STT generated by the transient thermal profile and SSE within the YIG layer. In these circumstances Eq. (1) is instead solved numerically.

Lateral heat diffusion at the surface of the sample may be ignored, because the laser spot diameter is much larger than the stack thickness. The transient temperature profile may then be obtained from a numerical solution of the one-dimensional

TABLE II. Assumed parameter values for optical and thermal calculations with an ambient temperature of 300 K. Values were taken from standard handbooks except where indicated otherwise.

Parameter	Al_2O_3	Py	Cu	YIG	GGG	Unit
density	3890	8700	8930	5170	7080	kg/m^3
thermal conductivity	1–4.5[a]	27[b]	150[c]	6.63[d]	7.94[d]	W/m/K
heat capacity	880	430	385	578	400	J/kg/K
refractive index n (800 nm)	1.759	$2.2 + j3.6$[e]	$0.24991 + j5.0337$	$2.19 + j2.48 \times 10^{-6}$[f]	1.95	
refractive index n (400 nm)				$2.74 + j0.36$[g]	2[h]	

[a]Reference [22].
[b]Reference [23].
[c]Reference [24].
[d]Reference [25].
[e]Reference [26].
[f]Reference [27].
[g]Reference [28].
[h]Reference [29].

heat diffusion equation

$$\frac{1}{D}\frac{\partial T}{\partial t} = \frac{\partial^2 T}{\partial z^2} + \frac{g(z,t)}{\kappa}, \tag{7}$$

where T is the temperature and $z = 0$ corresponds to the position of the interface between the Al cap and the underlying layer (either $Ni_{81}Fe_{19}$ or copper), with positive z corresponding to the direction into the substrate. The calculation assumes a single temperature for simplicity since the focus of the present study will be on magnetization dynamics that occur on time scales greater than 100 ps when the lattice and electron systems are assumed to be in mutual thermal equilibrium. A two-temperature model is generally required to describe the response to optical excitation on shorter time scales. Here D is the thermal diffusivity ($D = \kappa/\rho C_p$), κ is the thermal conductivity, ρ is the density, and C_p is the heat capacity per unit mass within a particular layer. The source term $g(z,t)$ describes the power density absorbed from the optical pump pulse. The source term is calculated from a multilayer transmission and reflection model for light propagation within a thin film [21]. Optical absorption is assumed to occur only within the lossy $Ni_{81}Fe_{19}$ and/or copper layers, with other layers in the stack being lossless, i.e., having negligible extinction coefficients (imaginary component of refractive index). The Al capping layer undergoes natural oxidation when exposed to atmosphere and is also assumed to be lossless. The ambient temperature before application of the pump pulse is assumed to be 300 K, while the parameters of individual layers used in the optical absorption and heat flow calculations are listed in Table II. The thermal boundary resistance values associated with the interfaces between different layers are not well known and may depend upon the detailed interface structure. A value of $1/R_{th} = 2.49\times10^8\ W/m^2/K$ was assumed for the Al_2O_3/Cu interface [30], while values of 2×10^8 and $1\times10^9\ W/m^2/K$ were deduced for Al_2O_3/$Ni_{81}Fe_{19}$ and $Ni_{81}Fe_{19}$/Cu, respectively. A value of $1/R_{th} = 2.04\times10^8\ W/m^2/K$ was assumed for YIG/GGG [31], while values of 2×10^8 and $1\times10^8\ W/m^2/K$ were deduced for Cu/YIG and Cu/GGG, respectively.

There is still debate about which features of the temperature profile are most important for the injection of spin current into the Cu layer by means of the SSE [32]. Therefore, both the change of temperature ΔT and the gradient ∇T were calculated throughout the structure of trilayer sample T1. The

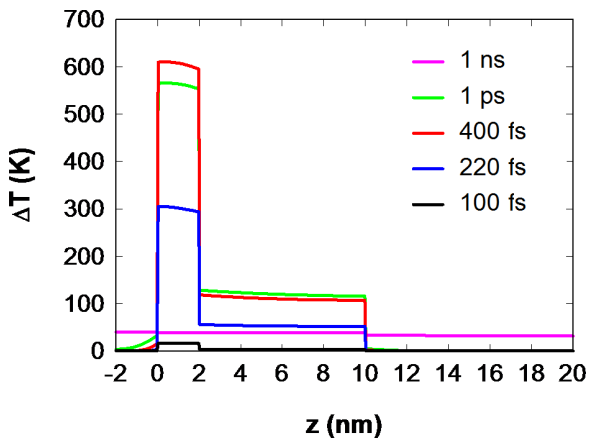

FIG. 2. Change in temperature ΔT as a function of position z within trilayer sample T1 at selected time delays for a pump fluence of $1.32\ mJ/cm^2$. The TBR has been included within the calculation.

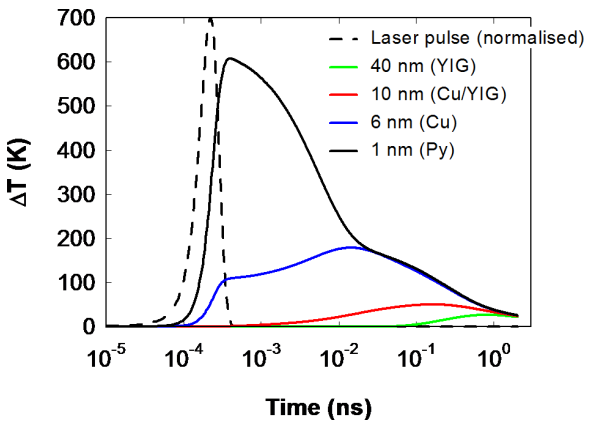

FIG. 3. Change of temperature ΔT as a function of time at selected positions within the trilayer sample T1. The curve plotted for a depth of 10 nm within the sample corresponds to the YIG side of the Cu/YIG interface. The TBR has been included within the calculation.

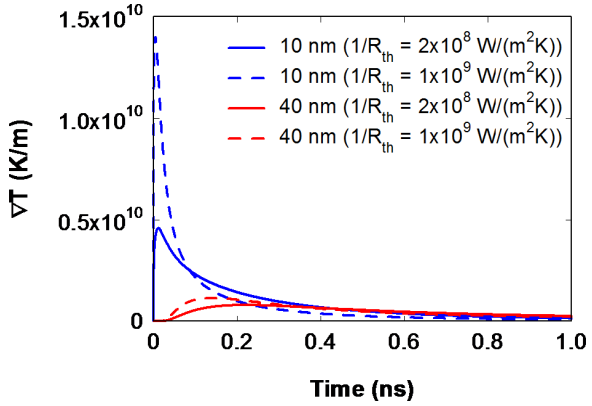

FIG. 4. Temperature gradient as a function of time for two positions within the YIG layer of the trilayer sample. The values assumed for the TBR at the Cu/YIG interface are shown within the legend.

spatial variation of ΔT in trilayer sample T1, induced by a pump pulse with fluence of 1.32 mJ/cm^2, is shown for selected times in Fig. 2. The time is measured from the peak value of the pump pulse, which is assumed to have a Gaussian temporal profile. The time dependence of ΔT at selected depths within the sample is shown in Fig. 3, specifically in the center of the $Ni_{81}Fe_{19}$ and Cu layers, at the Cu/YIG interface, and 40 nm below the Cu/YIG interface within the YIG. The temperature gradient at these last two positions is plotted in Fig. 4 for two different values of the thermal boundary resistance (TBR) at the Cu/YIG interface, demonstrating the sensitivity of the calculation to this parameter.

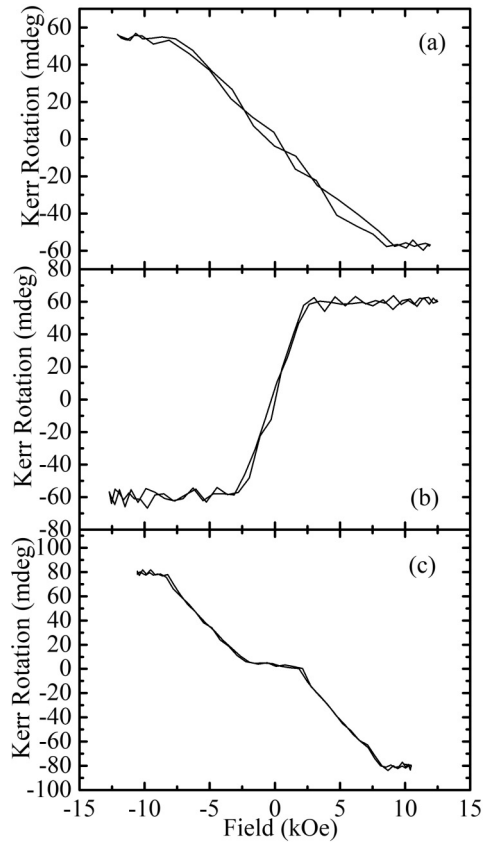

FIG. 5. Polar MOKE loops obtained from (a) the $Ni_{81}Fe_{19}$ reference sample R1, (b) the YIG reference sample R2, and (c) the trilayer sample T1, using ultrafast laser pulses of 400-nm wavelength. The magnetic field was applied parallel to the sample normal in (c) and at angle of 2.8° in (a) and (b).

IV. RESULTS

The magnetic anisotropy of the fabricated samples was first investigated by polar MOKE measurements using the 400-nm-wavelength probe beam generated by the ultrafast laser system as shown in Fig. 5. Polar MOKE loops obtained from the reference $Ni_{81}Fe_{19}$ (R1) and YIG (R2) films are shown in Figs. 5(a) and 5(b), respectively, while the loop for trilayer T1 is shown in Fig. 5(c). The observation of sharp saturation features for the two constituent layers within the trilayer indicates that there is negligible dipolar or exchange coupling between the two layers. Indeed, the observed saturation fields for the trilayer are similar to those observed for the reference samples. The saturation field H_{sat} corresponds to the effective demagnetizing field ($4\pi M_{eff}$) for a particular layer. In the case that there is negligible perpendicular anisotropy, of either bulk or interfacial origin, the saturation magnetization may be immediately calculated. Within pump-probe measurements the time-resolved MOKE (TRMOKE) signal in general contains contributions due to both reduction and reorientation of the magnetisation. Therefore, the reduction of the spontaneous magnetization was first determined from pump-probe measurements made with a magnetic field applied close to the sample normal, and of strength sufficient to quasialign the magnetization with the field, so as to suppress precession.

For all samples TRMOKE scans were measured for both positive and negative applied fields and the difference calculated to remove nonmagnetic effects. The difference scans are presented in Fig. 6. Figure 6(a) shows the TRMOKE response obtained from the GGG/YIG/Cu reference sample R2 with a field of 6.4 kOe applied normal to the sample plane. The maximum demagnetization, of up to about 3%, is observed at a time delay of around 0.7 ns. Since the YIG is transparent, the temperature within the YIG layer rises on a time scale of about 1 ns due to thermal conduction from the metallic overlayers, as shown in Fig. 3. Therefore, the reduction of the magnetization, and hence the demagnetizing field, has a rather long rise time and is ineffective in stimulating uniform precession within the YIG. This lack of precession, and the fact that the applied field is greater than the out-of-plane saturation value, justifies the assertion made in the theoretical consideration that the orientation of the YIG layer within trilayer samples can be considered fixed during pump-probe measurements. Figure 6(b) shows TRMOKE signals obtained from the $Ni_{81}Fe_{19}$ reference sample R1 for different pump fluences when a field of 12.4 kOe was applied parallel to the sample normal. The results of similar measurements made upon trilayer samples T1 and T3 are shown in Figs. 6(c) and 6(d), respectively. As expected, the demagnetization signal from the $Ni_{81}Fe_{19}$ rises on time scales of hundreds of femtoseconds and the response of the $Ni_{81}Fe_{19}$ dominates the signals obtained from the trilayer samples. A small-amplitude oscillation is superimposed upon the demagnetization signal in Fig. 6(c), indicating that precession has not been completely suppressed

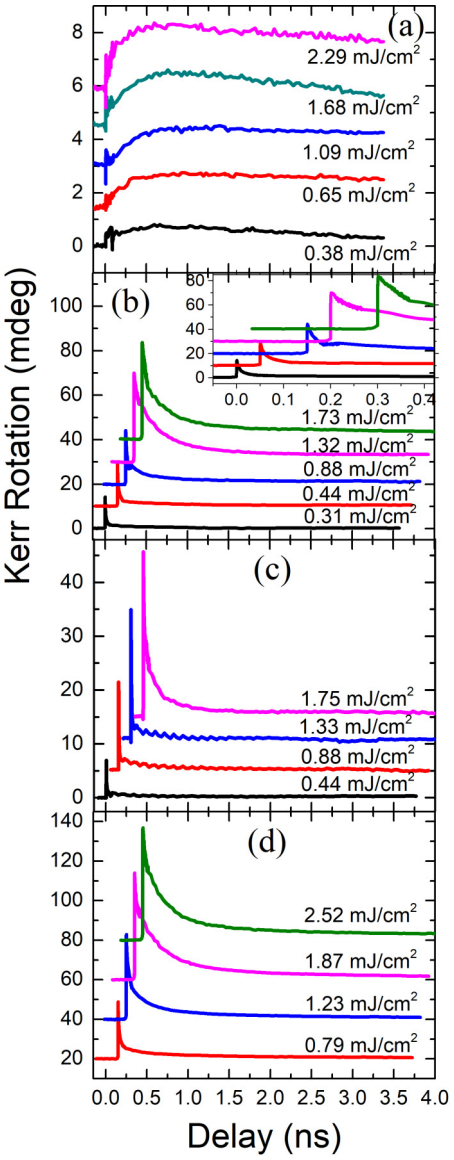

FIG. 6. TRMOKE measurements showing the optically induced reduction of the spontaneous magnetization, with data for different pump fluence values offset for clarity. Measurements were made with fields of (a) 6.4 kOe applied normal to the plane of the YIG reference sample R2, (b) 12.4 kOe applied normal to the $Ni_{81}Fe_{19}$ reference sample R1 (the inset has an expanded time axis), (c) 12.4 kOe applied normal to the trilayer sample T1, and (d) 13 kOe applied at 2.8° from the normal to the trilayer sample T3.

in this one case. The demagnetization response may still be extracted by smoothing the oscillatory component. Therefore, the data from Figs. 6(b)–6(d) provide a good estimate of the time dependence of the $Ni_{81}Fe_{19}$ saturation magnetization within samples R1, T1, and T3.

Although not clearly visible due to the range of the time axis in Fig. 6(a), the TRMOKE data for the YIG reference sample R2 exhibit high-frequency oscillations with frequency of about 95 GHz for time delays up to 0.1 ns. The raw scans acquired for positive and negative field polarities are shown in Fig. 7. A sharp peak is now observed at zero time delay with polarity that is unaffected by reversal of the applied magnetic

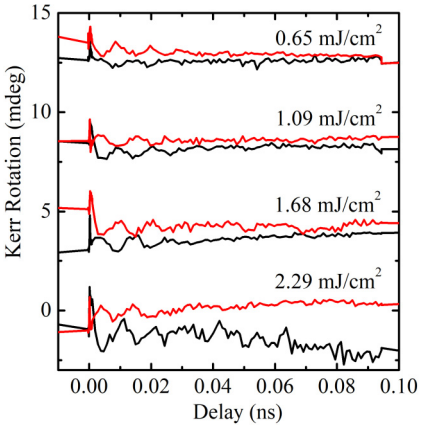

FIG. 7. TRMOKE data obtained from the YIG reference sample R2 for four different values of pump fluence. The red (black) curves were measured with a field of 6.4 kOe applied parallel to the positive (negative) z axis. The phase of oscillation is seen to change by π rad when the field is reversed.

field. This most likely arises from breakthrough of the transient reflectivity signal from the Cu layer into the rotation channel of the detector as a result of a slight misalignment of the incident probe beam polarization [19]. On longer time scales oscillations are observed that exhibit a phase shift of π rad when the magnetic field is reversed, suggesting that they are associated with a magnetic excitation rather than an acoustic phonon. Since the exchange modes of YIG have been predicted [33] and observed [34] to lie above 1 THz, it seems more likely that the mode observed in the present study is a dielectric mode with some coupling to the magnetization of the YIG [35]. The frequency of the dielectric mode is expected to depend upon the dimensions of the confining dielectric layer [36]. This may explain why the mode was observed in the thicker YIG layer of reference sample R2 but not within the thinner YIG layers of the trilayer structures. Given that the character of the mode is not known, the mechanism for its excitation is also unclear, but is unlikely to be associated with the thermal demagnetization of the YIG that occurs on longer time scales as shown in Fig. 6(a).

Measurements were next made with a field of variable strength applied at 2.8° relative to the sample normal. Figure 8 shows the TRMOKE signals acquired from the $Ni_{81}Fe_{19}$ reference sample R1 and trilayer samples T1, T2, and T3. The experimental data generally consist of an oscillatory response superimposed upon a multiexponential decaying background. To extract parameters such as the frequency and amplitude of oscillation and various relaxation times, the experimental data were fitted to an expression of the form

$$y = \frac{A}{2}\exp\left(\frac{w^2}{t_1^2} - \frac{t-t_0}{t_1}\right)\left[1 - \mathrm{erf}\left(\frac{w}{t_1} - \frac{t-t_0}{2w}\right)\right] + \frac{B}{2}\exp\left(-\frac{t-t_0}{t_2}\right)\left[1 + \mathrm{erf}\left(\frac{t-t_0}{2w}\right)\right] \times \cos[2\pi f(t-t_0) + 2\pi\beta(t-t_0)^2 + \phi] + C. \quad (8)$$

Here the first term describes an exponential relaxation of the sample convolved with Gaussian pump and probe pulses, where A is the amplitude, t_0 is the time at which the centers of

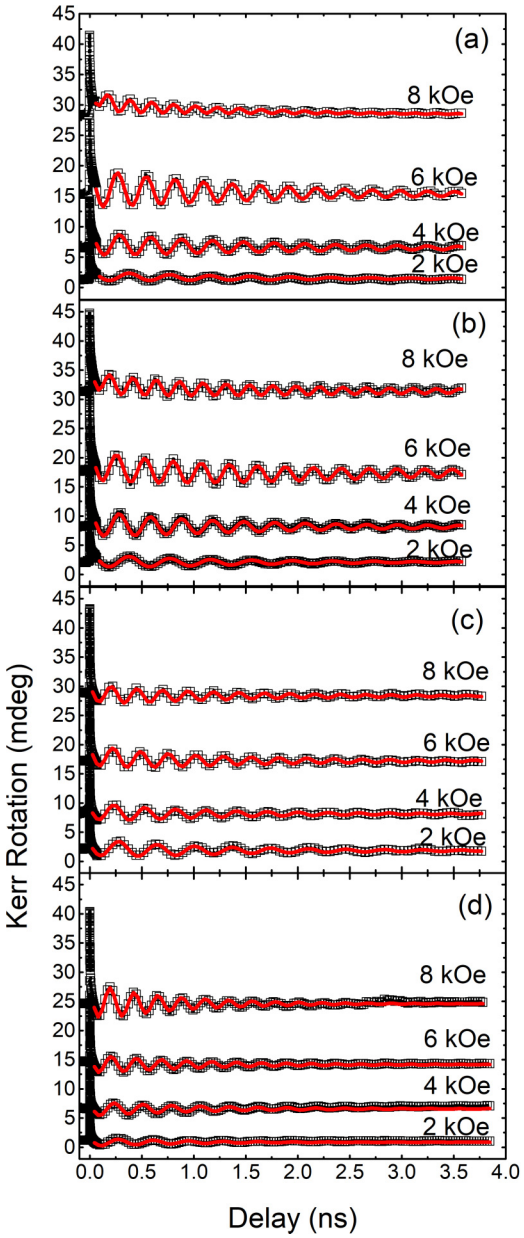

FIG. 8. TRMOKE signals recorded at different applied magnetic field values, with the field applied at 2.8° to the sample normal and for a fixed pump fluence of 0.66 mJ/cm^2, from (a) the $Ni_{81}Fe_{19}$ reference sample R1 and trilayer samples (b) T1, (c) T2, and (d) T3.

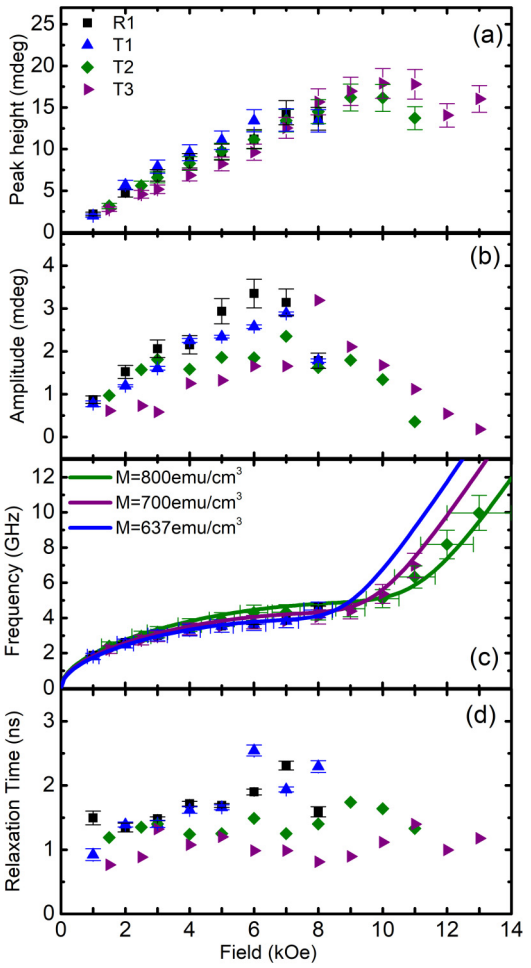

FIG. 9. Field dependence of parameter values extracted for samples R1 and T1–T3 from Fig. 8. (a) Ultrafast peak height measured from the raw experimental data. (b) Amplitude B, (c) frequency f, and (d) relaxation time t_2 of oscillation obtained by fitting the data of Fig. 8 to Eq. (8). The curves in (c) are calculated from Eqs. (4) and (6) for values of $g = 2$ and $M = 800$, 700, and 637 emu/cm^3.

the pump and probe pulses coincide at the sample, w defines the pulse width, t_1 is the relaxation time, and erf is the Gaussian error function. The second phenomenological term describes a damped oscillatory response of the sample, where B is the amplitude, f is the frequency of oscillation, t_2 describes the relaxation of the oscillatory component, β is a parameter that adds a linear chirp to the oscillation, and ϕ is the initial phase of the cosine oscillation. The third term with value C represents a constant offset. Equation (8) was fitted to the experimental data for positive values of the time delay immediately after the fall of the initial ultrafast demagnetization peak.

The TRMOKE signals acquired from samples R1 and T1–T3 at a fluence of 0.66 mJ/cm^2 for a range of field values are plotted in Fig. 8 and have been fitted to Eq. (8). The first term in Eq. (8) has amplitude A that tends to increase with field value and relaxation time t_1 that shows no clear field dependence, and is most likely associated with the recovery of the spontaneous magnetization. The third offset term is small and may arise from inductive pickup within the measurement electronics. The fitted parameter values from the second term are of principal interest here. The amplitude, frequency, and relaxation time of the oscillations have been plotted in Fig. 9, together with the height of the initial peak taken from the raw experimental data in Fig. 8. Although not plotted, a chirp parameter was generally required, reflecting a gradual change in frequency of order 0.01 GHz/ns that occurs as the sample temperature decreases and the spontaneous magnetization recovers. The phase of oscillation varied somewhat between different samples but was only weakly dependent upon the applied field value. Similar trends are observed in Fig. 9 for all four samples. The height of the ultrafast peak rises initially, but then appears to saturate near H_{sat}, as might be expected since the polar component of the magnetization dominates the measured signal. The oscillation amplitude is seen to increase

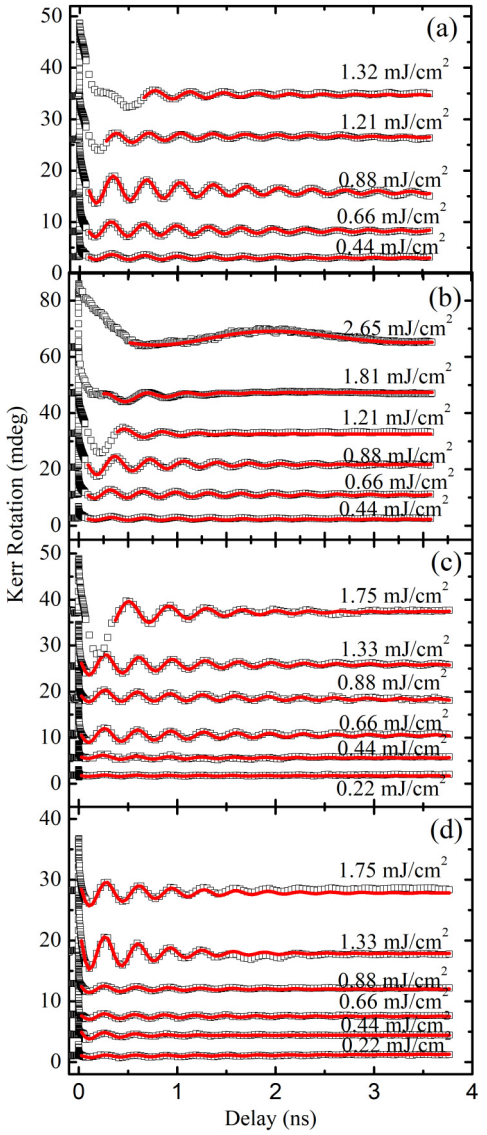

FIG. 10. TRMOKE data obtained for different pump fluence values, with a field of 3 kOe applied at an angle of 2.8° relative to the sample normal, for (a) the $Ni_{81}Fe_{19}$ reference sample R1 and trilayer samples (b) T1, (c) T2, and (d) T3.

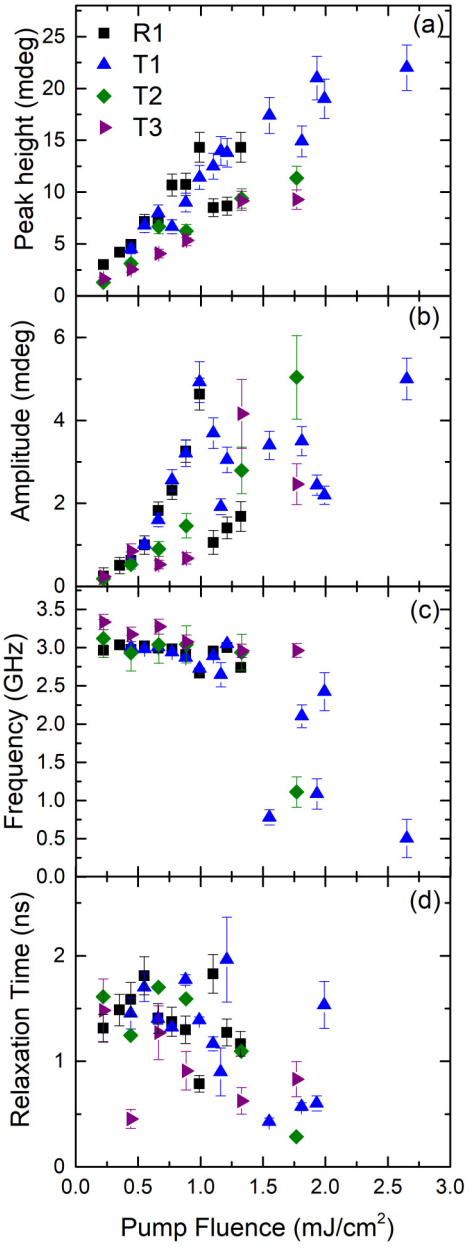

FIG. 11. Pump fluence dependence of parameter values extracted for samples R1 and T1–T3 from Fig. 10. (a) Ultrafast peak height measured from the raw experimental data. (b) Amplitude, (c) frequency, and (d) relaxation time t_2 of oscillation obtained by fitting the data of Fig. 10 to Eq. (8).

initially as the applied field is increased, reaching a maximum at a field value somewhat smaller than H_{sat} before decreasing as the field is increased further. There is a strong similarity in the field dependence of the frequencies obtained from the four samples, while the variation of the relaxation time t_2 is broadly similar for all samples. The t_2 relaxation times for samples R1, T1, and T2 are most similar at low field before becoming more scattered as the field increases towards H_{sat}. However, the relaxation times for sample T3 appear to be systematically smaller.

Figure 10 shows TRMOKE signals obtained from samples R1 and T1–T3 for different pump fluence values when a bias field of 3 kOe was applied at 2.8° from the normal to the plane of the sample. The red curves are fits to Eq. (8) and in each case begin from the time delay at which the sample response has settled into a simple damped oscillatory relaxation. For some large fluence values the first half cycle of oscillation exhibits an anomalous behavior and so has been excluded from the fitting. Measurements were performed in order of increasing pump fluence, with the measurement at the lowest fluence value being repeated after each increase in fluence. For sample T1 a noticeable change in the sample response at low fluence was first observed after exposure to a pump fluence of 2.65 mJ/cm^2, suggesting that this is the threshold value at which damage to the sample occurs. For the other samples the pump fluence remained sufficiently small that the damage threshold was not reached.

The parameter values obtained from the TRMOKE data of Fig. 10 are shown in Fig. 11. The ultrafast demagnetization

peak is seen to exhibit a roughly linear increase with pump fluence for all samples, with values that are generally larger for R1 and T1 compared to T2 and T3. Deviations from the monotonic trend, e.g., between 1 and 1.25 mJ/cm^2 for sample R1, may indicate some drift in the overlap of the pump and probe spots upon the sample surface. The variation in peak height observed between different samples, which is generally similar to that observed in Fig. 9, may reflect differences in the optical constants of the four samples that influence the absorption of the pump pulse. The oscillation amplitude shows a more complicated behavior. For T2 and T3, the samples that received the piranha etch, the amplitude increases slowly at first but then rises dramatically when the fluence exceeds 1 mJ/cm^2, whereas for R1 and T1 the amplitude increases more strongly for low fluence before decreasing above 1 mJ/cm^2. It should be noted that the excitation and evolution of precessional oscillations depend upon the temperature of the $Ni_{81}Fe_{19}$ layer at times after the rise of the ultrafast demagnetization peak. The temperature profile and its temporal evolution are sensitive to the thermal parameters of the stack, which may vary between samples and may have a nonlinear dependence upon the pump fluence. Therefore, the complicated variation of the precession amplitude may not be surprising. On the other hand, the frequency and relaxation time t_2 of the oscillatory response show similar behavior for all samples up to a fluence of about 1.5 mJ/cm^2. In this region the frequency decreases gradually with increasing fluence, while the relaxation time decreases more strongly with some outlying data points. For example, the anomalously small relaxation time t_2 for sample T3 at a fluence of 0.44 mJ/cm^2 occurs because the oscillatory signal does not exhibit a simple exponential decay in this case. Beyond a fluence of 1.5 mJ/cm^2 both frequency and relaxation time show increased scatter. From Fig. 10, the phase of oscillation (not plotted in Fig. 11) shows only a weak dependence upon pump fluence until a threshold of 1.21, 1.21, and 1.33 mJ/cm^2 for R1, T1, and T2, respectively, whereas a threshold does not appear to be reached for T3. Again, the fitted chirp parameter, also not shown, corresponds to a frequency decrease of order 0.01 GHz/ns.

In order to gain greater insight into the origin of the observed precessional oscillations, numerical solutions of Eq. (1) were first calculated for the simplest structure, the $Ni_{81}Fe_{19}$ reference film R1. Excitation by the pump pulse leads to an initial modification of the magnetic parameters of the sample on a time scale that is short compared to the period of precession. These same parameters then relax more gradually towards their ambient values with increasing time delay. As a first approximation, the Gilbert damping parameter α and the spectroscopic splitting factor g were assumed to be independent of time delay with values of 0.01 and 2, respectively. The spontaneous magnetization varies strongly with time delay. An ambient value of 637 emu/cm^3 was determined from the out-of-plane saturation field in Fig. 5(a), while the time dependence of the magnetization was obtained by linear interpolation between the fluence values used for measurements with a large out-of-plane field shown in Fig. 6(b). Any volume or surface-type magnetocrystalline anisotropy was assumed to be negligible. The numerical solution yields the time-dependent magnetization, which may then be turned into a Kerr rotation, for comparison with the experimental data, by normalizing the out-of-plane component of magnetization to the height of the polar hysteresis loop.

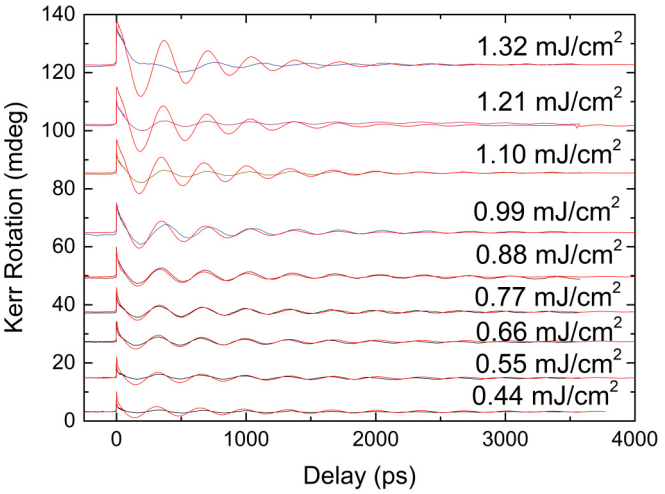

FIG. 12. Simulated (red curves) and TRMOKE data for different pump fluences for the $Ni_{81}Fe_{19}$ reference sample R1. The assumed time dependence of the magnetic parameters is described in the text.

For small values of the pump fluence it was found that good agreement between the phase of the measured and calculated oscillations could be obtained by adding 10% of the longitudinal magnetization component (i.e., the component that lies both in the plane of the sample and within the plane of optical incidence) to the polar magnetization component in the simulation, as shown in Fig. 12. Some contribution from the longitudinal Kerr effect is expected when the probe beam is incident at 15° to the sample normal, but its size relative to the polar Kerr signal has a complicated dependence upon the optical parameters of the different layers within the sample and is not easily calculated from first principles. Indeed, this may explain the small but noticeable difference in phase values observed between the samples R1 and T1–T3. The frequency and phase of the oscillations are in reasonable agreement for all but the largest fluence value, where the assumption that the damping parameter is independent of delay time may become inadequate. This suggests that the numerical macrospin solution of Eq. (1) may be used to obtain a qualitative understanding of the trilayer sample response to STT generated by means of the SSE as long as the pump fluence is not too large.

Solution of Eq. (1) for the trilayer samples requires that the time dependence of the STT terms be known. Neglecting the fieldlike term, the amplitude of the antidamping torque a is assumed to be proportional to the spin current J_s generated by the SSE. At present, there is no consensus as to whether the spin current is driven by the temperature difference across the YIG/Cu interface, shown in Fig. 2, which depends strongly upon the thermal boundary resistance, or the temperature gradient shown in Fig. 4, which depends strongly upon the position z relative to the surface of the sample. In either case the calculated temporal dependence is complicated and subject to assumptions made about the parameters shown in Table II. Clearly, a STT that exhibits a supralinear decrease with increasing time will have the greatest influence upon the short time-scale dynamics and influence the phase of

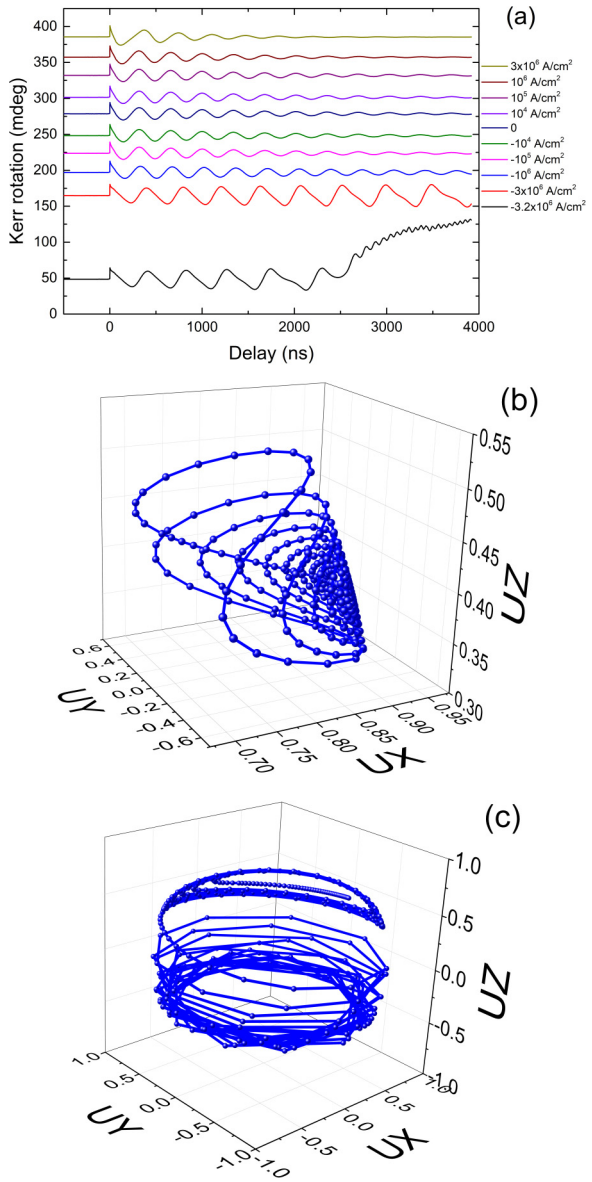

FIG. 13. (a) Calculated TRMOKE signals for different spin current densities stated in charge units of A/cm^2. Also shown is the trajectory of the $Ni_{81}Fe_{19}$ layer magnetization for spin current densities of (b) $J_s = -10^4$ A/cm^2 and (c) $J_s = -3.2\times10^6$ A/cm^2.

precession more strongly than its subsequent damping. Since the measurements of Fig. 10 did not show any systematic variation of this phase, it is more fruitful to consider the precessional oscillations that occur on longer time scales. Calculations were performed for the simplest case, in which the time dependence of the STT is described by a Heaviside (step) function, as shown in Fig. 13, in order to establish an upper bound for the magnitude of the STT operating on these time scales. Again, the $Ni_{81}Fe_{19}$ layer was assumed to have $g = 2$ and $\alpha = 0.01$, while its magnetization was assumed to have the same time dependence as for sample R1 in Fig. 12, and 10 % of the longitudinal magnetization component was included in the calculation of the magneto-optical response. In the absence of spin current the $Ni_{81}Fe_{19}$ magnetisation exhibits a damped elliptical precession about its equilibrium orientation. Increasing the spin current density with positive sign leads to increased damping of the precession, while a spin current density of negative sign leads to reduced damping. In both cases, the phase of oscillation changes gradually with the magnitude of the spin current. Beyond a threshold value of order -10^6 A/cm^2 the damping is fully compensated and the amplitude of precession begins to increase with time until the magnetization switches to a new trajectory for which the magnetization precesses about the normal to the plane of the sample.

V. DISCUSSION

The optically induced dynamics of trilayer and reference single-layer structures have been presented for different values of the pump fluence and applied field in Figs. 6–8 and 10. All the structures containing a $Ni_{81}Fe_{19}$ layer (R1 and T1–T3) show clear precessional oscillations of the $Ni_{81}Fe_{19}$ magnetization that are induced by ultrafast demagnetization when the static magnetization of the $Ni_{81}Fe_{19}$ is canted with respect to the applied field. In contrast, the YIG does not exhibit uniform mode precession because it demagnetizes more slowly (∼100 ps) by means of the spin-lattice interaction. The frequency of precession of the $Ni_{81}Fe_{19}$ is well described by an analytical solution of the linearized Landau-Lifshitz equation as shown in Fig. 9. Both the polar saturation field, shown in Fig. 5, and the field dependence of the precession frequency depend upon the effective $4\pi M$ thin-film demagnetizing field. These measurements suggest that the effective demagnetizing field is somewhat smaller for samples R1 and T1 compared to T2 and T3, for which the surface of the YIG was etched before deposition of the metallic layers. The difference may result from a difference in the spontaneous magnetization of the $Ni_{81}Fe_{19}$ layer, or surface anisotropy at its interfaces that we have hitherto ignored, or perhaps due to roughness or discontinuities in the structure of the $Ni_{81}Fe_{19}$ layer.

For the trilayer structures, numerical solutions of the full Landau-Lifshitz equation presented in Fig. 13 clearly show that the relaxation time of the precessional oscillations should be noticeably modified by the presence of STT generated by the SSE as the magnitude of the spin current density increases from 10^4 to 10^5A/cm^2. The relaxation of the precessional oscillations is shown in Figs. 8 and 10, while the extracted relaxation times are shown in Figs. 9 and 11. There is no conclusive systematic difference between the damping of the oscillations in R1, T1, and T2, at least for pump fluences up to 1.5 mJ/cm^2, while there is a general tendency towards greater damping in T3. Since there is no YIG layer in R1, it therefore seems unlikely that there is significant STT generated by the SSE within any of the samples studied here. Rather, the larger damping within T3 may be associated with pumping of spins into the Cu spacer layer by the precessing Py magnetization, which are scattered strongly by the inserted Ta layer. There are more significant differences in the behavior of the TRMOKE signals acquired at the largest fluences shown in Fig. 10. Notably, the phase of the first half cycle of oscillation may be modified. However, a very similar effect was again observed for both samples R1 and T1, and attempts to reproduce this phase shift using our simple model proved to be unsuccessful. On the other hand, since irreversible changes were observed in the response of T1 for a fluence of 2.56 mJ/cm^2, the

high-fluence behavior may also be influenced by reversible structural changes induced by the pump pulse. A more detailed understanding of such effects is required to understand the observed variations in phase.

The thermal modeling presented in Figs. 2–4 shows that excitation by femtosecond laser pulses may induce transient temperature changes of hundreds of degrees Kelvin and temperature gradients of up to 10^{10} K/m that exceed those realized in conventional transport measurements by many orders of magnitude. Although the values of many of the parameters used in the modeling are poorly known, one might still expect the STT generated by the SSE to be maximized in such experiments. The lack of any evidence for STT influencing the dynamics observed in this study suggests that either the YIG/Cu interface is ineffective in transmitting spin current in the present samples or the spin current generated by the LSSE during the first few nanoseconds after optical excitation has magnitude of order 10^4 A/cm^2 or smaller. The former explanation seems unlikely since YIG/Pt samples fabricated in the same growth system have exhibited spin Hall magnetoresistance [37], current drive ferromagnetic resonance with a spin-orbit torque contribution [38], and large dc inverse spin Hall effect voltages when precession was excited in the YIG [39]. Therefore, high spin transmissivity can also be expected at the YIG/Cu interfaces studied here.

Recent static studies of the LSSE in YIG/metal thin film structures have considered the variation of the LSSE coefficient $\sigma_{\mathrm{LSSE}} = V_{\mathrm{LSSE}} L_z/(L\Delta T)$, where V_{LSSE} is the voltage induced along a planar strip of the metal with length L and L_z is the total thickness of the layers supporting the temperature difference ΔT. It was found that σ_{LSSE} increases with YIG thickness but then saturates when the thickness exceeds the average propagation length of the thermal magnons [40], which was determined by Guo *et al.* to be about 1 μm at 300 K [32]. Guo *et al.* also observed that σ_{LSSE} exhibited a maximum at a temperature that increased with decreasing YIG thickness. As the temperature is reduced the magnon propagation length increases, causing σ_{LSSE} to increase, until it becomes limited by the thickness of the YIG. Further reduction of temperature leads to a smaller population of thermal magnons with fixed propagation length so that σ_{LSSE} then decreases. The same authors also observed that σ_{LSSE} was reduced when a 2-nm Cu layer was inserted between YIG and Pt layers, suggesting that interface structure influences the transmission of the spin current.

From these published LSSE measurements it is possible to estimate the magnitude of the spin current generated within the optically stimulated measurements presented here. Guo *et al.* obtained a value of $\sigma_{\mathrm{LSSE}} \sim 0.03\,\mu$V/K at 300 K for a YIG film of 150 nm thickness with an overlayer of Pt of thickness $d_{\mathrm{Pt}} = 5$ nm. They also stated values of $\theta_H = 0.068$, $\rho_{\mathrm{Pt}} = 0.42\,\mu\Omega$m, and $\lambda_{\mathrm{Pt}} = 2$ nm for the spin Hall angle, resistivity, and diffusion length of the Pt, respectively. The associated spin current density, expressed in charge units, is then given approximately by $J_S = \sigma_{\mathrm{LSSE}} d_{\mathrm{Pt}} \nabla T/(\theta_{\mathrm{Pt}}\rho_{\mathrm{Pt}}\lambda_{\mathrm{Pt}})$. A thermal gradient ∇T of 2×10^9 K/m, similar to that which might be expected close to the Cu/YIG interface from Fig. 4, then yields a spin current density of order 5×10^3 A/cm^2. From Fig. 13, this is about an order of magnitude too small to have a noticeable effect upon the damping of the precession reported in the present work. While the strength of the SSE may be increased substantially in thicker films at temperatures of about 100 K [32], this is unlikely to be attractive for applications in data storage technology. Instead it may be more productive to adjust the thermal parameters of the stack so as to sustain a larger temperature gradient within the YIG layer.

Heating by femtosecond laser pulses can also generate significant temperature differences across a YIG/metal interface because optical absorption occurs preferentially within the metal. In the recent study of Kimling *et al.* [10], which employed pump fluences comparable to those in the present study, it was inferred that a temperature difference of order 10 K can be generated across the YIG/metal interface over time scales of order 100 ps. For YIG/Cu, the spin current density was found to be equal to the temperature difference across the interface multiplied by a factor of approximately 3×10^8 A m^{-2} K^{-1}. From Fig. 3, calculated for a pump fluence of 1.32 mJ/cm^2, the temperature difference across the Cu/YIG interface corresponds to the difference of the curves plotted for depths of 6 and 10 nm and is at a maximum value of order 100 K after 10 ps, corresponding to a maximum spin current density of 3×10^6 A/cm^2, before decreasing to the order of 1 K after 1 ns. This should manifest as a deviation from simple exponential damping, with noticeably different damping during the first few hundred picoseconds. However, the data in Figs. 8 and 10 are well described by simple exponential damping, while Figs. 9 and 11 do not suggest any significant difference in damping between sample R1 and samples T1 and T2. It may be that the TBR, and hence the temperature difference across the Cu/YIG interface, is smaller than assumed in our calculations or that the spin transmissivity of the interface is smaller for our samples. Improved understanding of the interface is required to produce larger temperature differences simultaneously with high spin transmissivity so that useful torques may be obtained.

In summary, the optically induced dynamics of YIG/Cu/$Ni_{81}Fe_{19}$ spin valves and YIG and $Ni_{81}Fe_{19}$ reference structures have been investigated in ultrafast pump-probe measurements. While the precessional dynamics of the $Ni_{81}Fe_{19}$ can be well understood in terms of a simple macrospin model, there is no evidence for the presence of STT associated with spin current generated by means of the LSSE within the YIG layer. The experimental approach developed here may be useful in exploring other structures in which a fuller consideration of thermal and interfacial properties may be used to generate larger thermal gradients and interfacial temperature differences and hence larger spin currents.

ACKNOWLEDGMENTS

The authors gratefully acknowledge financial support from Engineering and Physical Sciences Research Council Grant No. EP/J018767/1 and an EPSRC CASE award with Dr. D. Williams of Hitachi Cambridge. H.J.M. acknowledges financial support in the form of a scholarship from "The Establishment of Martyrs of Iraq."

[1] T. Kimura, J. Hamrle, and Y. Otani, Phys. Rev. B **72**, 014461 (2005).

[2] Y. K. Kato, R. C. Myers, A. C. Gossard, and D. D. Awschalom, Science **306**, 1910 (2004).

[3] J. Wunderlich, B. Kaestner, J. Sinova, and T. Jungwirth, Phys. Rev. Lett. **94**, 047204 (2005).

[4] H. Adachi, K. Uchida, E. Saitoh, and S. Maekawa, Rep. Prog. Phys. **76**, 036501 (2013).

[5] K. Uchida, S. Takahashi, K. Harii, J. Ieda, W. Koshibae, K. Ando, S. Maekawa, and E. Saitoh, Nature (London) **455**, 778 (2008).

[6] C. M. Jaworski, J. Yang, S. Mack, D. D. Awschalom, J. P. Heremans, and R. C. Myers, Nat. Mater. **9**, 898 (2010).

[7] K. Uchida, J. Xiao, H. Adachi, J. Ohe, S. Takahashi, J. Ieda, T. Ota, Y. Kajiwara, H. Umezawa, H. Kawai, G. E.W. Bauer, S. Maekawa and E. Saitoh, Nature (London) **9**, 894 (2010).

[8] D. Meier, D. Reinhardt, M. van Straaten, C. Klewe, M. Althammer, M. Schreier, S. T. B. Goennenwein, A. Gupta, M. Schmid, C. H. Back, J.-M. Schmalhorst, T. Kuschel, and G. Reiss, Nat. Commun. **6**, 8211 (2015).

[9] M. Weiler, M. Althammer, F. D. Czeschka, H. Huebl, M. S. Wagner, M. Opel, I.-M. Imort, G. Reiss, A. Thomas, R. Gross, and S. T. B. Goennenwein, Phys. Rev. Lett. **108**, 106602 (2012).

[10] J. Kimling, G.-M. Choi, J. T. Brangham, T. Matalla-Wagner, T. Huebner, T. Kuschel, F. Yang, and D. G. Cahill, Phys. Rev. Lett. **118**, 057201 (2017).

[11] J. C. Slonczewski, Phys. Rev. B **82**, 054403 (2010).

[12] A. J. Schellekens, K. C. Kuiper, R. R. J. C. de Wit, and B. Koopmans, Nat. Commun. **5**, 4333 (2014).

[13] G.-M. Choi, B.-C. Min, K.-J. Lee, and D. G. Cahill, Nat. Commun. **5**, 4334 (2014).

[14] G.-M. Choi, C.-H. Moon, B.-C. Min, K.-J. Lee, and D. G. Cahill, Nat. Phys. **11**, 576 (2014).

[15] S. M. Rezende, R. L. Rodríguez-Suárez, R. O. Cunha, A. R. Rodrigues, F. L. A. Machado, G. A. Fonseca Guerra, J. C. Lopez Ortiz, and A. Azevedo, Phys. Rev. B **89**, 014416 (2014).

[16] M. B. Jungfleisch, V. Lauer, R. Neb, A. V. Chumak, and B. Hillebrands, Appl. Phys. Lett. **103**, 022411 (2013).

[17] A. Mitra, O. Cespedes, Q. Ramasse, M. Ali, S. Marmion, M. Ward, R. M. D. Brydson, C. J. Kinane, J. F. K. Cooper, S. Langridge, and B. J. Hickey, Sci. Rep. **7**, 11774 (2017).

[18] A. Ghosh, S. Auffret, U. Ebels, and W. E. Bailey, Phys. Rev. Lett. **109**, 127202 (2012).

[19] R. Wilks, R. J. Hicken, M. Ali, B. J. Hickey, J. D. R. Buchanan, A. T. G. Pym, and B. K. Tanner, J. Appl. Phys. **95**, 7441 (2004).

[20] E. Beaurepaire, J.-C. Merle, A. Daunois, and J.-Y. Bigot, Phys. Rev. Lett. **76**, 4250 (1996).

[21] A. W. Crook, J. Opt. Soc. Am. **38**, 954 (1948).

[22] S.-Y. Bai, Z.-A. Tang, Z.-X. Huang, J. Yu, and J.-Q. Wang, Chin. Phys. Lett. **25**, 593 (2008).

[23] A. D. Avery, S. J. Mason, D. Bassett, D. Wesenberg, and B. L. Zink, Phys. Rev. B **92**, 214410 (2015).

[24] L. Wenjun, Y. Yang, and M. Asheghi, in *Proceedings of the Tenth Intersociety Conference on Thermal and Thermomechanical Phenomena in Electronics Systems* (IEEE, Piscataway, NJ, 2006), p. 1171.

[25] A. M. Hofmeister, Phys. Chem. Miner. **33**, 45 (2006).

[26] G. Neuber, R. Rauer, J. Kunze, T. Korn, C. Pels, G. Meier, U. Merkt, J. Bäckström, and M. Rübhausen, Appl. Phys. Lett. **83**, 4509 (2003).

[27] T. Goto, M. C. Onbaşlı, and C. A. Ross, Opt. Express **20**, 28507 (2012).

[28] B. Abdel Samad, M.-F. Blanc-Mignon, M. Roumie, A. Siblini, J. P. Chatelon, and M. Korek, Eur. Phys. J. Appl. Phys. **50**, 10502 (2010).

[29] D. L. Wood and K. Nassau, Appl. Opt. **29**, 3704 (1990).

[30] B. C. Gundrum, D. G. Cahill, and R. S. Averback, Phys. Rev. B **72**, 245426 (2005).

[31] M. Schreier, A. Kamra, M. Weiler, J. Xiao, G. E. W. Bauer, R. Gross, and S. T. B. Goennenwein, Phys. Rev. B **88**, 094410 (2013).

[32] E.-J. Guo, J. Cramer, A. Kehlberger, C. A. Ferguson, D. A. MacLaren, G. Jakob, and M. Kläui, Phys. Rev. X **6**, 031012 (2016).

[33] J. Barker and G. E. W. Bauer, Phys. Rev. Lett. **117**, 217201 (2016).

[34] A. J. Princep, R. A. Ewings, S. Ward, S. Tóth, C. Dubs, D. Prabhakaran, and A. T. Boothroyd, arXiv:1705.06594.

[35] S. Parchenko, T. Satoh, I. Yoshimine, F. Stobiecki, A. Maziewski, and A. Stupakiewicz, Appl. Phys. Lett. **108**, 032404 (2016).

[36] M. A. Popov, I. V. Zavislyak, and G. Srinivasan, J. Appl. Phys. **110**, 024112 (2011).

[37] S. R. Marmion, M. Ali, M. McLaren, D. A. Williams, and B. J. Hickey, Phys. Rev. B **89**, 220404(R) (2014).

[38] Z. Fang, A. Mitra, A. L. Westerman, M. Ali, C. Ciccarelli, O. Cespedes, B. J. Hickey, and A. J. Ferguson, Appl. Phys. Lett. **110**, 092403 (2017).

[39] C. J. Durrant, S. Marmion, B. J. Hickey, and R. J. Hicken (unpublished).

[40] A. Kehlberger, U. Ritzmann, D. Hinzke, E.-J. Guo, J. Cramer, G. Jakob, M. C. Onbasli, D. H. Kim, C. A. Ross, M. B. Jungfleisch, B. Hillebrands, U. Nowak, and M. Kläui, Phys. Rev. Lett. **115**, 096602 (2015).